Au-rich filamentary behavior and associated subband gap optical absorption in hyperdoped Si

W. Yang,[1] A. J. Akey,[2] L. A. Smillie,[1] J. P. Mailoa,[3] B. C. Johnson,[4] J. C. McCallum,[4] D. Macdonald,[5] T. Buonassisi,[3] M. J. Aziz,[2] and J. S. Williams[1]

[1]*Research School of Physics and Engineering, The Australian National University, Canberra, ACT 2601, Australia*
[2]*Harvard John A. Paulson School of Engineering and Applied Sciences, Cambridge, Massachusetts 02138, USA*
[3]*Massachusetts Institute of Technology, Cambridge, Massachusetts 02139, USA*
[4]*School of Physics, University of Melbourne, Melbourne, VIC 3010, Australia*
[5]*Research School of Engineering, The Australian National University, Canberra, ACT 2601, Australia*

(Received 25 April 2017; published 22 December 2017)

Au-hyperdoped Si, synthesized by ion implantation and pulsed laser melting, is known to exhibit a strong sub-band gap photoresponse that scales monotonically with the Au concentration. However, there is thought to be a limit to this behavior since ultrahigh Au concentrations ($>1 \times 10^{20}$ cm^{-3}) are expected to induce cellular breakdown during the rapid resolidification of Si, a process that is associated with significant lateral impurity precipitation. This work shows that the cellular morphology observed in Au-hyperdoped Si differs from that in conventional, steady-state cellular breakdown. In particular, Rutherford backscattering spectrometry combined with channeling and transmission electron microscopy revealed an inhomogeneous Au distribution and a subsurface network of Au-rich filaments, within which the Au impurities largely reside on substitutional positions in the crystalline Si lattice, at concentrations as high as ∼3 at. %. The measured substitutional Au dose, regardless of the presence of Au-rich filaments, correlates strongly with the sub-band gap optical absorptance. Upon subsequent thermal treatment, the supersaturated Au forms precipitates, while the Au substitutionality and the sub-band gap optical absorption both decrease. These results offer insight into a metastable filamentary regime in Au-hyperdoped Si that has important implications for Si-based infrared optoelectronics.

DOI: 10.1103/PhysRevMaterials.1.074602

I. INTRODUCTION

The unparalleled technological maturity of silicon could be exploited to develop complementary-metal-oxide-semiconductor-compatible optoelectronics such as near-IR photodetectors and imaging arrays [1]. These applications require the realization of a sub-band gap photoresponse in Si, as the low-attenuation wavelengths commonly used in fiber optics (up to $\lambda \sim 1650$ nm) fall below its 1.12-eV band gap ($\lambda < 1100$ nm). Without the need for complex heterostructures or waveguides [2,3], a promising method for achieving the sub-band gap photoresponse is to add an intermediate band (IB) within the band gap by incorporating appropriate impurities into the Si lattice [4]. This approach would allow sub-band gap photons to excite electrons from the valence band (VB) to the IB, and then from the IB to the conduction band (CB). Achieving this form of IB requires a high concentration of impurities (often beyond the thermodynamic equilibrium solubility limit) since the localized, discrete impurity levels must interact and broaden into a delocalized band [5]. The IB must also be well separated from both the CB and the VB, and be partially filled to enable electronic transitions.

The high impurity concentration required for IB formation can, in principle, be achieved by ion implantation and pulsed laser melting (PLM), a combination of methods giving rise to a nonequilibrium process known as "hyperdoping" [6]. Following PLM, the ion implanted layer regrows as a single crystal via liquid-phase epitaxy, during which the implanted impurities become incorporated into the regrown Si as a result of rapid, nonequilibrium resolidification from the melt [7–9]. To date, two classes of impurities for synthesizing hyperdoped IB Si have been investigated. Chalcogens (S, Se, and Te), when used to hyperdope Si, give rise to strong sub-band gap optical absorption [10–12], but this is not translated into high photoconductivity [13]. In fact, the IB introduced by chalcogens overlaps with the CB and becomes fully filled, resulting in an insulator-to-metal transition [13,14]. Consequently, free-carrier absorption overwhelms the sub-band gap photoresponse at room temperature unless the material is counterdoped with another impurity such that the Fermi level is lowered [15,16]. The second class of impurities for hyperdoping Si is transition metals, many of which naturally create partially filled, deep levels in the band gap [17,18]. Indeed, a room-temperature infrared photodetector based on Au-hyperdoped Si has been demonstrated [19]. Although the external quantum efficiency was low, substantial improvement in efficiency was predicted if higher Au concentrations could be incorporated.

Several factors have been found to limit the degree of attainable substitutional impurity concentration, but the most common one is the well-known phenomenon of cellular breakdown [20,21], which is a manifestation of the high impurity concentration in the bulk liquid that destabilizes the moving liquid-solid interface through constitutional undercooling [22,23]. As the interface roughens, impurities segregate laterally with respect to the main solidification front and form characteristic cellular features [24]. Such cell walls were shown to extend a few hundred nanometers into the solidified layer and contained laterally segregated impurities that create "channels" of a precipitate phase, bounding columns of single crystalline Si inside the cells [25,26]. For this reason, the impurity concentration at the onset of cellular breakdown was generally considered to be the upper limit for the concentration of impurities that can be incorporated into substitutional lattice sites [18,27].

A more complex microstructure following resolidification, however, was recently revealed by Akey *et al.* in cobalt-hyperdoped Si that exhibited the early stages of interface instability yet had not given rise to conventional cellular breakdown [28]. Instead of showing precipitate-decorated cell walls as previously reported for conventional cellular breakdown, atom probe tomography revealed a filamentary, inhomogeneous distribution of highly concentrated Co (up to ∼10 at. %) in single-phase diamond-cubic Si with a thin layer of cell-like structure at the surface, suggesting a novel compositional regime in hyperdoped Si.

In this work, we show that, in Si hyperdoped with Au by ion implantation and PLM, the supersaturated Au distribution is likewise inhomogeneous at high Au concentrations, yet the Au dopants remain highly substitutional in the Si lattice. We demonstrate that the sub-band gap absorptance in the hyperdoped layer continues to increase with increasing substitutional Au dose even after the onset of the inhomogeneous morphology containing Au-rich filaments. Furthermore, after rapid thermal annealing at temperatures beyond 400°C, the Au is found to precipitate and the enhancement in absorption diminishes correspondingly. These results provide further insight into this metastable compositional regime, in which segregated Au in the Au-rich regions exhibits significant substitutionality and corresponding optical activity.

II. EXPERIMENT

A. Sample preparation

Samples were prepared by implanting Au^+ ions with a range of implant energies (50–300 keV) into ⟨100⟩ oriented *n*-type Si wafers (double-side polished, phosphorus doped, resistivity 1–10 Ω cm) at liquid nitrogen temperature in vacuum for ion doses ranging from 3×10^{14} to 8×10^{15} cm^{-2}. Au implantation was performed at 7° to the surface normal to avoid ion channeling effects. All samples, except those implanted at 50 keV, were subsequently melted, in air, by a single laser pulse from a Nd:YAG laser operating at 355 nm with a pulse duration of 5 ns FWHM, at laser fluences ranging from 0.7 to 1.0 J cm^{-2}. Samples implanted at 50 keV were melted in air by a single laser pulse from a XeCl laser operating at 308 nm, with a pulse duration of 25 ns FWHM and a laser fluence of 1.7 J cm^{-2}. At these laser fluences, the Au-rich amorphous layer resolidifies via liquid-phase epitaxy. *In situ* time-resolved reflectivity (TRR) measurements during PLM show that the melt duration ranged from 35 to 55 ns.

For the thermal stability analysis, samples implanted with 300-keV 6×10^{15} cm^{-2} Au and subjected to PLM were subsequently annealed using a Jipelec rapid thermal annealing (RTA) furnace, at nominal temperatures ranging from 400°C to 750°C for 3 min in a flowing Ar ambient. One sample was annealed at 750°C for 10 min. We note that the actual temperatures reached may be up to 100°C lower than the nominal temperature as a result of difficulties with temperature measurement in the RTA system at that time, but this does not affect the results presented below since no quantitative analysis is attempted.

B. Characterization

Rutherford backscattering spectrometry combined with ion channeling (RBS/C) was carried out on all samples using a 2.0-MeV He^+ beam at the Australian National University (ANU). A glancing exit angle of 12° was used to achieve the desired depth resolution. To calculate Au substitutionality, RBS spectra were obtained for the laser-melted samples from both the ⟨100⟩ axial channel direction and a random direction. As-implanted regions were also analyzed.

Scanning electron microscopy (SEM) and cross-sectional transmission electron microscopy (XTEM) were used to characterize the surface and subsurface morphology of the hyperdoped layers, respectively. The SEM used was a FEI Verios FESEM system with a 2-keV electron beam operating in immersion mode. TEM examination used two JEOL JEM-2100F instruments operating at 200 keV. Conventional TEM, selected-area electron diffraction (SAED), nanobeam electron diffraction (NBED), and high-resolution imaging were performed on one instrument. The other instrument was used to perform energy-dispersive x-ray spectroscopy (EDS) using an Oxford X-MaxN 80T EDXS detector with the instrument operating in the scanning transmission electron microscopy (STEM) mode, as well as for additional NBED measurements. Preparation of the TEM samples was by the dimpling and ion-polishing method with final thinning performed using a 2-keV Ar beam. In some cases, samples were plasma-cleaned before TEM examination.

The sub-band gap absorption of the Au-hyperdoped samples was quantified by measuring the total hemispherical (both specular and diffused) transmittance (T) and reflectance (R) using a PerkinElmer Lambda 1050 UV/Vis/NIR spectrophotometer with an integrating sphere detector in the near-infrared wavelengths of interest ($\lambda = 1000 - 1800$ nm). The absorptance (A) was then deduced based on $A = 1 - T - R$. An InGaAs detector was used with a gain of 0.15 and a response time of 0.80 s. For each sample, the values of measured transmittance T and reflectance R were the numerical averages of three separate sets of measurements on different laser-melted regions within one laser spot. A white Spectralon reference block is used for calibration. The errors in the T and R measurements are estimated to be $\pm 0.25\%$ (absolute).

III. RESULTS AND DISCUSSION

A. Inhomogeneous Au distribution

In this section, we show characterization results for the 300-keV implants melted with a 0.78 J cm^{-2} laser fluence to illustrate the typical behavior of Au-hyperdoped Si following PLM. Under these conditions, embryo cellular structures begin to emerge at the surface for Au implant doses as low as 1×10^{15} cm^{-2}, as illustrated in Fig. 1 by SEM. The surface cells then become better defined with increasing Au dose. The general appearance of the cells is consistent with previous reports on transition-metal-hyperdoped Si that had undergone cellular breakdown, in which the surface cell walls are shown to be decorated with segregated or precipitated impurities [18,29,30]. However, as we demonstrate below, this surface cellular structure does not necessarily imply a subsurface

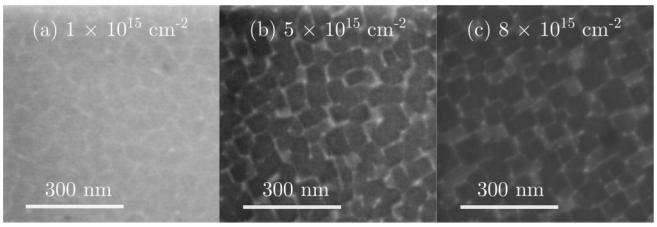

FIG. 1. Cellular surface structures observed on Au-hyperdoped Si at implanted Au doses of (a) 1×10^{15} cm^{-2}, (b) 5×10^{15} cm^{-2}, and (c) 8×10^{15} cm^{-2} (300-keV implant, ~0.78 J cm^{-2} laser fluence).

cellular network for Au in Si. As an example, we show two such cases by examining the subsurface structure by XTEM.

Figure 2(a) shows a TEM image of a cross section of the resolidified layer with a Au implant dose of 2×10^{15} cm^{-2}, illustrating the characteristic featureless microstructure of single-crystalline, defect-free Si. As this sample exhibited surface cells similar to those in Fig. 1, the featureless XTEM clearly indicates that a surface cell structure does not necessarily indicate a subsurface cellular network. Indeed, such surface features are more likely to originate from the very last stages of the resolidification, as we discuss later. In contrast, at the Au implant dose of 6×10^{15} cm^{-2}, shown in Fig. 2(b), the surface cell structures coexist with subsurface dark regions that correspond to higher average mass and extend to the surface. The subsurface dark regions are shown to be Au rich in the subsequent EDS map [Fig. 2(c)]. A comparison between the cross-sectional EDS map of the Au signal (shown in green) and the XTEM image taken from a similar region of the sample (i.e., around a Au-rich filament), as shown in Figs. 2(b) and 2(c), confirms that these inhomogeneous and disconnected regions contain laterally segregated Au. The filaments have a higher but variable Au concentration compared with the surrounding material, in particular the lighter-colored "columns" between filaments. A similar behavior is observed for all implant doses in this study, with the total area of the Au-rich regions increasing as the Au dose increases. We conclude that while the cell walls on the surface have previously been interpreted as laterally segregated components of subsurface vertical cells that extend a few hundred nanometers below the surface, the segregation

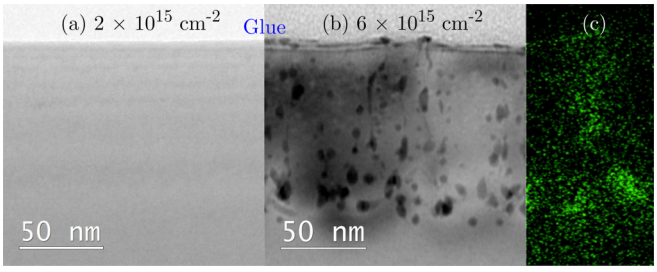

FIG. 2. (a) XTEM image of a sample implanted to 2×10^{15} cm^{-2} at 300 keV and pulsed laser melted at 0.78 Jcm^{-2}. (b) XTEM image of a sample implanted to 6×10^{15} cm^{-2} at 300 keV and pulsed laser melted at 0.78 Jcm^{-2}. (c) EDS map of a single vertical filament of segregated Au, taken from a region different from but qualitatively identical to (b), with the same depth and scale bar as (b).

behavior observed in the XTEM images in Fig. 2 does not support this interpretation in this Au implant dose regime. Despite the inhomogeneous Au distribution, the crystalline Si surrounding the Au-rich regions remains defect free, with no evidence of silicide or precipitate formation in the SAED patterns, as shown in the Supplemental Material (Fig. S1) [31]. Thus, although lateral Au segregation during solidification gives rise to Au-rich filaments, it does not result in Au precipitation in these regions. Rather, the Au concentration in the filaments is less than 10 at. %, as estimated in Sec. 2 of the Supplemental Material [32].

To further investigate the inhomogeneous behavior of Au in the hyperdoped Si layer, we employed RBS/C to quantify the Au distribution normal to the surface and the substitutionality of the inhomogeneous Au. Figures 3(a)–3(c) show the RBS spectra for samples hyperdoped with Au to 2×10^{15}, 4×10^{15}, and 6×10^{15} cm^{-2}, respectively, before and after PLM. Before PLM, the as-implanted RBS/C spectra (red squares) show amorphous layers of 250, 280, and 330 nm for the three Au doses, respectively. Within the amorphous layers, the Au distribution is roughly Gaussian while the underlying Si substrate remains single crystalline and Au free.

By examining the random RBS results first, after PLM, the Au distribution profiles (black triangles) are seen to shift toward the surface and a significant fraction of the Au appears to have segregated to the surface. The redistribution of the Au upon solidification can be described by the classical segregation theory, with Au atoms being rejected into the liquid ahead of the solidifying liquid-solid interface because Au is more soluble in the liquid phase than in the solid phase [33]. Simultaneously, the high solidification velocity following PLM, estimated to be ~7 ms^{-1} for identical PLM conditions [18], is comparable to the diffusive velocity of Au at the crystal-melt interface and traps a large fraction of the Au in the solidified Si lattice [8,33]. As a result, a supersaturated solid solution with Au concentrations that exceed the equilibrium solid solubility limit by orders of magnitude is formed, as has been widely observed previously [26,34]. However, at high Au implant doses, the Au distribution after PLM shows marked differences from that observed for doses at and below 2×10^{15} cm^{-2}, which we discuss below.

In contrast to the sample implanted to 2×10^{15} cm^{-2} (or below), where a relatively constant Au distribution is contained within the resolidified layer along with a prominent Au surface peak, broadened peaks at depths of ~110 nm are observed for samples with higher Au doses (4×10^{15} and 6×10^{15} cm^{-2}), as shown in Figs. 3(b) and 3(c). In these latter cases, a smaller fraction of the Au is segregated to the surface. These subsurface peaks indicate regions with very high local Au concentration, consistent with the XTEM images in Fig. 2, where inhomogeneous branches of Au-rich regions are only observed for doses above 2×10^{15} cm^{-2}. Quantitative analysis of the RBS spectra using the RUMP software package [35] indicates that the near-constant subsurface Au concentration for the sample implanted to 2×10^{15} cm^{-2} is ~0.5×10^{20} cm^{-3} (0.1 at. %). At the higher doses of 4×10^{15} and 6×10^{15} cm^{-2}, peak Au concentrations of ~2×10^{20} cm^{-3} (0.4 at. %) and ~7×10^{20} cm^{-3} (1.4 at. %) are obtained. Somewhat surprisingly, the Au concentration at the onset of the Au-rich filamentary behavior agrees with the calculated threshold concentration

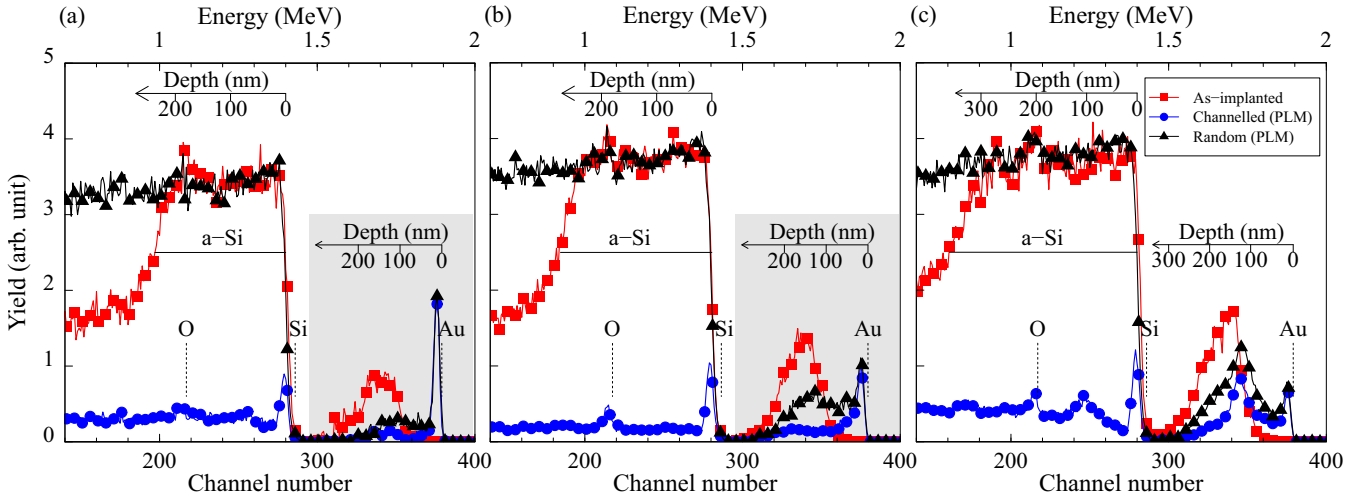

FIG. 3. RBS/C spectra for Au-hyperdoped Si implanted at (a) a Au dose of 2×10^{15} cm^{-2}, with the Au yield (shown in grey) magnified by a factor of 3 for visual clarity; (b) a Au dose of 4×10^{15} cm^{-2}, with the Au yield (shown in grey) magnified by a factor of 2 for visual clarity; and (c) a Au dose of 6×10^{15} cm^{-2}. The as-implanted RBS/C spectra are shown as red squares while the random and channeled spectra after PLM (laser fluence 0.78 J cm^{-2}) are shown in black and blue, respectively. We note that a thin layer of native oxide on the surface for all samples gives rise to the labeled oxygen peak.

for cellular breakdown to occur for Au in Si (1×10^{20} cm^{-3}) [18,27]. However, we stress that, while samples implanted to 2×10^{15} and 1×10^{15} cm^{-2} show surface cellular structures in SEM, they do not contain any significant subsurface microstructure, disorder, or inhomogeneity within the resolution of TEM. Furthermore, at the higher Au concentrations where filamentary behavior was clearly observed, the XTEM data do not reveal any evidence for continuous, vertical subsurface cell walls, or for the precipitation of Au into crystallites within the Si lattice.

Examining now the RBS/C spectra in Fig. 3 following PLM (blue circles), all three samples exhibit excellent recrystallization as shown by the low Si yield. However, a subsurface disorder peak can be observed at ∼110 nm below the surface, which indicates a small amount of residual disorder within the resolidified lattice. This effect is particularly prominent for the highest dose of 6×10^{15} cm^{-2}. It is interesting to note that the depth of this disorder peak corresponds to the depth of the subsurface Au peak for this sample, suggesting that the incorporation of the very highly concentrated Au distorts or disorders the surrounding host Si lattice. Such a behavior might be expected from the considerable difference in atomic radius between Si and Au atoms. The degree of Au substitutionality in the resolidified layer can be approximated by normalizing the ratio between the integrated RBS yield of the channeled and random Au signal to the corresponding Si integrated yields, determined over the same depth. Specifically, the substitutional fraction f_{sub} is given by [36]

$$f_{\text{sub}} = \frac{1 - \frac{X_{\text{Au\_}c}}{X_{\text{Au\_}r}}}{1 - \frac{X_{\text{Si\_}c}}{X_{\text{Si\_}r}}}$$

where $X_{\text{Au\_}c}$ and $X_{\text{Au\_}r}$ are, respectively, the channeled and random Au yield integrated over the resolidified depth (excluding the surface), while $X_{\text{Si\_}c}$ and $X_{\text{Si\_}r}$ are the corresponding Si yields, integrated over the same depth. For the sample implanted to 2×10^{15} cm^{-2}, this calculation indicates ∼60% of the Au that is trapped in the Si following PLM (i.e., below the surface) resides in near-substitutional lattice positions. However, somewhat unexpectedly, for samples implanted to 4×10^{15} and 6×10^{15} cm^{-2}, despite the inhomogeneity in the Au distribution both laterally and in depth, the substitutional fraction below the surface (∼60% and ∼50%, respectively) remains similar to that of the 2×10^{15} cm^{-2} case. Furthermore, high-resolution XTEM images, as shown in Figs. S2 and S3, on samples implanted to 6×10^{15} and 8×10^{15} cm^{-2}, show that the lattice fringes from regions around the Au-rich filaments deviate slightly from those of the surrounding Si lattice [37]. Such features are suggestive of strain, but there are no extended defects emanating from the filamentary regions.

The structural characterization of Au-hyperdoped Si described above reveals an interesting Au segregation regime that leads to filamentary branches of Au-rich regions rather than the subsurface cell structure and precipitation that characterize conventional cellular breakdown [24]. We examine the key differences between these regimes below.

First, we discuss the observation of surface cells at low Au doses in which no subsurface microstructure following PLM is observed. In these cases, the surface cells are clearly not lateral extensions of subsurface vertical cells. Indeed, the lack of contrast in the XTEM images shown in Fig. 2(a) implies a laterally uniform Au distribution subsurface. Thus, we suggest that, during the final stages of solidification, the Au that is segregated to the surface concentrates laterally into Au-rich cells at the surface, possibly aided by a lower melting temperature of Au-rich Si. However, the mechanism for such a process is not understood and further studies are needed.

When the implanted Au dose, and hence the Au concentration, is sufficiently high, subsurface Au-rich filaments emerge in addition to the surface cells. At such Au concentrations, interface instability occurs as a result of the segregated Au fraction at the moving melt-solid interface, as any fluctuations

in the Au concentration along the interface would amplify as a function of time [27]. Yet, the high Au substitutionality and the single-crystalline structure within the observed Au-rich regions suggest that the time available for amplification, i.e., the resolidification time, is too short to allow for the precipitation of a second phase. Instead, an inhomogeneous structure containing a considerable concentration of dissolved Au is formed. This observation further emphasizes that the segregation regime studied here is not steady state and likely occurs at lower Au concentrations than are necessary for conventional cellular breakdown.

The short resolidification time is also consistent with our observation of local lattice distortions around the Au-rich filaments and the lack of extended defects in the resolidified layer. It is significant to highlight crystal twinning during resolidification and surface undulations observed in the sample implanted to 8×10^{15} cm^{-2}, where greater interface instability might be anticipated. In fact, twin formation is likely to result from a rough solidification front [38], which is enhanced by Au-induced melting point suppression, consistent with previous observations where nonplanar interfaces and associated twin formation resulted from rapid solidification of implantation-amorphized ⟨111⟩ oriented Si. This is further supported by the fact that such twin formation rarely emanates from the Au-rich filaments.

The interface breakdown dynamics in this transient filamentary regime has been previously discussed by Akey *et al.* in relation to Co-hyperdoped Si [28]. In both Co- and Au-hyperdoped Si, the impurity-rich regions are formed as a result of constitutional undercooling, as described previously, during which the impurity-rich regions at the solidifying interface stay molten for longer than the surrounding regions. By quantifying the difference in peak Au concentration between the low- and high-dose samples, as measured by RBS, and estimating the volume of the Au-rich filaments, we confirm that the average Au concentration in the filaments is ∼3 at. % [39]. This value is quantitatively consistent with that measured in Co-rich filaments (6 at. %) [28]. We note that the filamentary segregation pattern observed here is analogous to the pattern observed in Co-hyperdoped Si, although the Au-rich regions appear to be more disconnected. Thus, as previously identified [28], we attribute the discontinuous morphology of the impurity-rich regions to a pinch-off mechanism, in which a Rayleigh instability in the molten, impurity-rich regions amplifies by impurity bulk diffusion and results in local breakups in the molten threads of impurity, so as to minimize the interfacial energy [40]. The effect of "pinching" in the Au-rich regions appears to be more pronounced than in the Co-rich material, presumably because of the higher diffusivity of Au in molten Si and the stronger impurity-induced melting point suppression associated with Au in Si [41].

In summary, at the Au concentrations studied in this work, we have uncovered a regime following PLM that is qualitatively different from conventional cellular breakdown. Specifically, we have shown that in this regime (i) a surface cellular structure does not necessarily imply a subsurface cellular network; (ii) the Au distribution becomes laterally inhomogeneous as the Au concentration increases; (iii) the Au-rich filaments consist of around 3 at. % Au dissolved in good-quality, single-crystalline Si; and (iv) these highly concentrated Au regions cause lattice distortion but the Au atoms are mostly substitutional. This high substitutionality of Au inside the Au-rich regions is significant in terms of optical properties since substitutional Au has previously shown to be directly related to enhanced sub-band gap absorption in Au-hyperdoped Si [19]. Hence, it is interesting to study whether the very high substitutional Au fractions we observe in samples that exhibit filamentary behavior translate into high sub-band gap optical absorption, as investigated below.

B. Near-infrared optical absorption

To study the optical activity of the Au dopants in all samples (at Au concentrations both below and above the inhomogeneous Au distribution regime), we measured the optical absorptance of samples fabricated using different implant energies and/or different laser fluences. Such sets of implant and PLM conditions result in different effective layer thicknesses and degrees of surface segregation (a higher laser fluence results in a longer melt duration and, hence, more segregation towards the surface). Because undoped Si has negligible optical absorptance in the wavelength range being measured here [as shown in Fig. 4(a)], we assume that the Au-free substrate does not contribute to the sub-band gap absorption and that the enhancement in infrared absorption comes from the Au-hyperdoped layer only.

Figure 4(a) shows the absorptance from 1000 to 1800 nm for the Au-hyperdoped samples as well as for the undoped reference samples. Note that the absorptance of the pristine Si sample is the same as that of a Si self-implanted sample that has also resolidified following PLM, confirming that the enhanced absorption does not arise from possible damage from either the implantation or the PLM process, an observation that is consistent with previous reports [10,19]. In Fig. 4(a) the absorptance increases monotonically as the Au dose increases. This trend is consistent with previous observations on lower dose samples which did not show surface cellular structures [19]. However, given that the Au distribution is inhomogeneous for doses above 2×10^{15} cm^{-2}, the continually increasing absorptance for such cases is noteworthy. In fact, using the method outlined by Mailoa *et al.* [19], the average absorption coefficient α for the hyperdoped layer for a 6×10^{15} cm^{-2} sample is estimated to be 5200 cm^{-1} at 1300 nm, which is more than eight times the best result from the previous study (600 cm^{-1}) [19], and more than three times that of the sample doped to 2×10^{15} cm^{-2}, which did not show any signs of inhomogeneous subsurface Au distribution (1600 cm^{-1}). We also emphasize that, because of the inhomogeneous Au distribution, the Au is mostly concentrated within the top 110 nm of the hyperdoped layer. Hence, the absorption coefficient in these localized regions could be more than a factor of 3 higher than the average over the entire resolidified layer.

We next ask why the inhomogeneous Au distribution does not appear to limit the sub-band gap absorption. In the previous study on Au-hyperdoped Si by Mailoa *et al.* [19], a kink in spectral response at a photon energy of 0.78 eV ($\lambda = 1590$ nm) was shown to be related to a well-known donor level introduced by substitutional Au at 0.78 eV from the conduction band [43,44]. When the Au concentration is low, the enhanced sub-band absorption can only be detected at

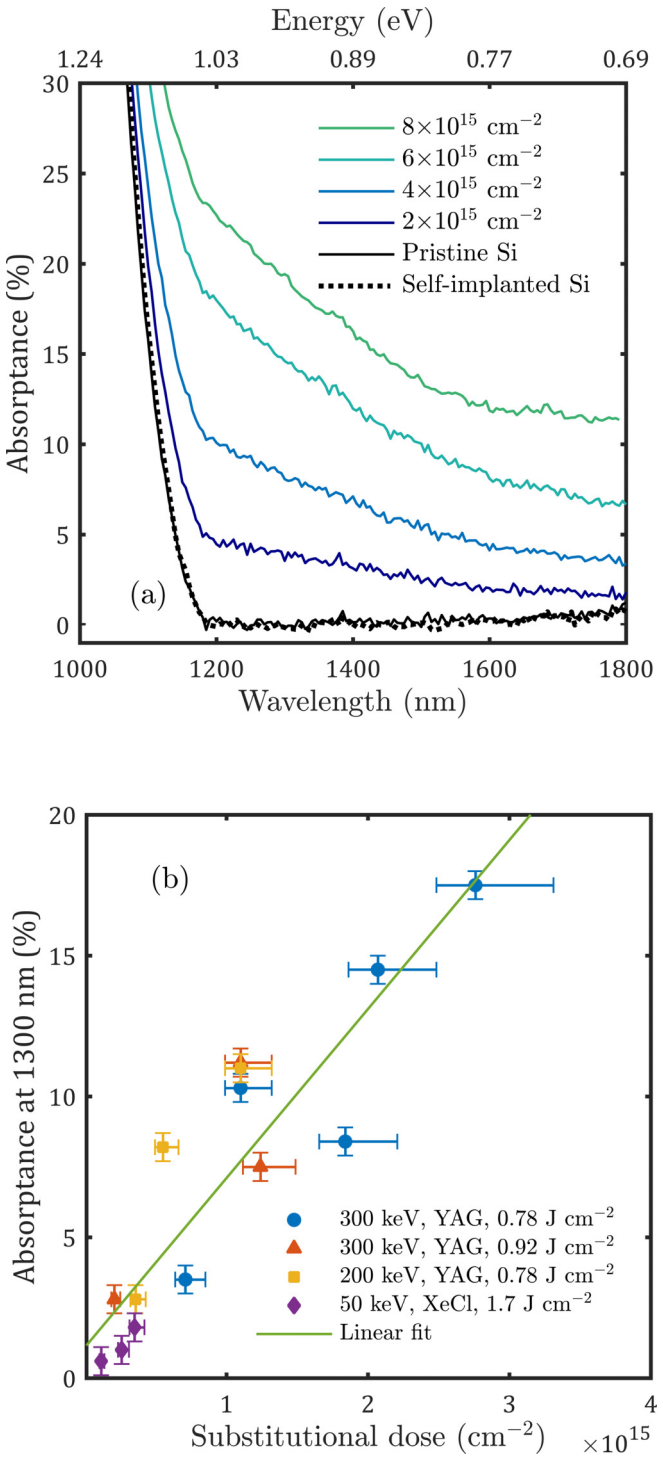

FIG. 4. (a) Sub-Band gap optical absorptance of Au-hyperdoped Si implanted at various energies and at various Au doses. The absorptance of an undoped pristine Si sample, as well as one that is self-implanted with 110-keV Si^+ ions to 2×10^{15} cm^{-2} (the peak concentration of Si in this sample is comparable with the peak concentration of Au achieved in the hyperdoped samples) then melted under identical laser conditions, are shown as references. Note that the absorptance increases smoothly after ~1600 nm in the reference samples due to free carrier absorption in *n*-type Si [42]. (b) Absorptance at 1300 nm plotted against substitutional Au dose, obtained from different samples. A line of best fit is shown in green.

liquid nitrogen temperature due to overwhelming free-carrier absorption at higher temperatures. As the Au concentration increases, these discrete donor levels interact and extend into a donor band, giving rise to sub-band gap absorption that is observable at room temperature. In view of the high substitutional Au concentrations observed here, despite the onset of inhomogeneous Au-rich regions, we suggest that the increased optical absorption can also be explained in terms of the 0.78-eV donor band, which continues to widen as the substitutional Au dose increases. Indeed, Fig. 4(b) illustrates that the sub-band gap optical absorptance exhibits a roughly linear dependence on the total substitutional Au dose. Although the data show some scattering, there is an obvious increasing trend in the absorptance, which only depends on the substitutional Au dose and does not appear to depend on the thickness of the resolidified layer (independent of implant energy) or the degree of surface Au segregation (independent of laser fluence). Moreover, the absorption also appears to be largely independent of the degree of homogeneity of the Au distribution and the occurrence, or otherwise, of cellular surface features.

C. Thermal deactivation

Our analysis of the Au-rich regions so far suggests that the inhomogeneous Au is likely to be non-steady state and thus highly metastable. To gain further insight into the thermal stability of Au-hyperdoped Si after the onset of the inhomogeneous behavior, the sample doped to 6×10^{15} cm^{-2} was isochronally annealed at a range of different temperatures for 3 min. Below 400°C, RBS/C data show that both the total Au distribution and the substitutionality of the Au do not change significantly. At annealing temperatures higher than 400°C, however, the Au starts to move off lattice positions into nonsubstitutional sites, as RBS/C reveals very little substitutional Au is left (~2%) after RTA at 750°C for 3 min. Figure 5 shows the RBS/C Au signal taken from both the random and channeled directions, before and after RTA at 750°C, juxtaposed with the corresponding XTEM images.

Along with the decrease in Au substitutionality, XTEM micrographs also indicate extensive Au precipitation during subsequent RTA. As shown in the XTEM image in Fig. 5(a), following PLM, the Au concentration is laterally uniform at depths >110 nm from the surface (yellow circles), since no contrast is observed in the XTEM. However, after subsequent RTA, small dark spheres emerge in this region and extend roughly to the maximum melt depth, which defines the extent of Au supersaturation. Additionally, at depths <110 nm from the surface (red circles), the Au that originally segregated into inhomogeneous Au-rich regions after PLM appears to have evolved into well-defined spherical precipitates. Although we show only one annealing temperature in Fig. 5, we have examined the XTEM micrographs and Au profiles of various samples after annealing at different temperatures, and the general behavior is similar to that in Fig. 5(b). However, it was found that more precipitates accumulated at the surface as the annealing temperature is increased. In addition, Ostwald ripening, driven by surface energy considerations, becomes evident to a small degree as the annealing temperature is

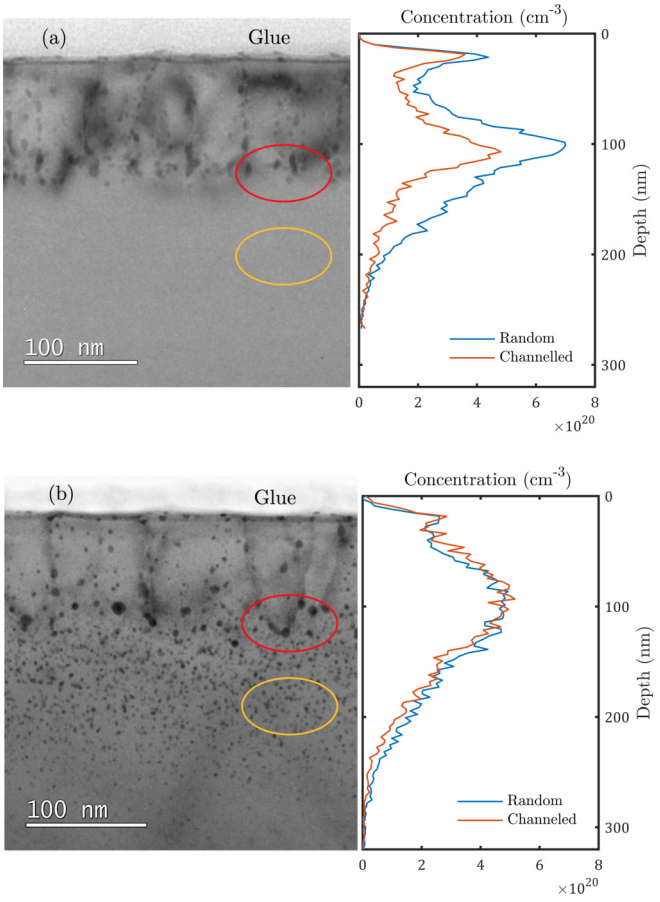

FIG. 5. XTEM images shown alongside the corresponding random and channeled Au profiles as measured by RBS/C of (a) the PLM sample implanted to 6×10^{15} cm^{-2} after PLM and (b) the same sample after RTA at 750°C for 3 min. Circles, drawn at the same depths in both samples, highlight the structural changes induced by annealing.

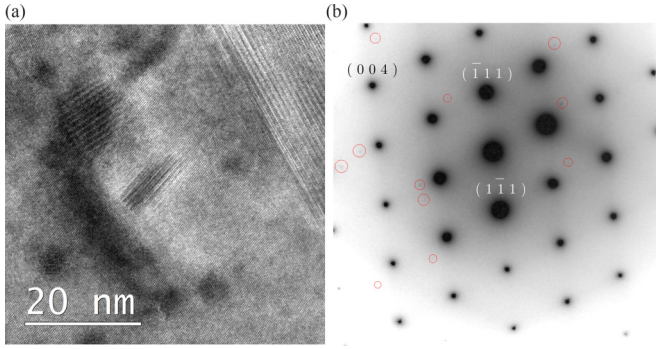

FIG. 6. (a) HRTEM image of the dark, spherical regions, as shown in Fig. 5(b), after RTA at 750°C for 3 min. (b) SAED taken on the dark spheres, from the (011) zone axis, gives rise to additional weak reflections (highlighted by red circles).

increased, resulting in the growth of larger precipitates at the expense of the smaller ones, and a slight broadening of the Au profile, as shown in Fig. 5(b) [45]. Finally, there is a strong correlation between the loss of Au substitutionality, as measured by RBS/C, and the emergence and growth of the precipitates.

Further characterization of the dark spherical precipitates was performed by high-resolution XTEM (HRTEM) to elucidate their nature. Figure 6(a) shows that, due to the presence of Moiré fringes, the lattice planes within the precipitates do not all align perfectly with the surrounding single-crystalline Si, or with each other. SAED on such regions, shown in Fig. 6(b), reveals additional diffraction spots, marked by red circles, that do not correspond with diamond-cubic Si and suggests the formation of another—possibly metastable Au silicide—phase. We conclude that the Au-rich filaments observed in the hyperdoped layers following PLM readily evolve into well-defined precipitates upon subsequent thermal annealing, which are hypothesized to be Au silicide. We also note that the precipitated phase could not be unambiguously identified from the position and spacing of diffraction spots. Because the annealing temperatures (>450°C) are higher than the Au-Si eutectic temperature of 363°C, we expect the Au-rich filaments to have melted during annealing, giving rise to the round, randomly oriented precipitates on cooling [46]. It is interesting to note that a similar phase has been previously observed on Au-supersaturated Si formed by furnace annealing (at much lower Au concentrations), where spherical, orthorhombic Au silicide forms upon subsequent thermal relaxation [47].

Accompanying the Au precipitation and the concomitant decrease in substitutionality, we would expect the sub-band gap optical absorptance to also decrease with increasing annealing temperature. This is confirmed by optical absorption measurements on PLM samples subsequently annealed by RTA at different temperatures, as shown in Fig. 7(a). In light of the sub-band gap absorption mechanism described in the previous section, this reduction in absorptance can be attributed to the decrease in substitutional Au dose. After being annealed at 750°C for 10 min, the sub-band gap absorptance does not diminish completely even though the substitutionality is effectively zero in the resolidified layer (as measured by RBS/C). This behavior is not unexpected since, during RTA, there is sufficient time for Au to diffuse throughout the wafer, a process consistent with that commonly observed during furnace heat treatments of Si containing a high Au content [17,48]. In particular, during annealing, substitutional Au diffuses through the wafer at a concentration equal to the equilibrium solubility limit at the respective annealing temperature, and excess Au above this limit is gettered to, and precipitates at, suitable (defect) sites, or at the wafer surfaces [46]. If the Au optical activity is controlled by the amount of substitutional Au in the wafer, we would expect the absorption after RTA to reflect the substitutional Au content *throughout* the wafer. Note that the equilibrium solid solubility limit of substitutional Au in Si is $\sim 1 \times 10^{14}$ cm^{-3} at 750°C [49], and, given that the sample was reasonably rapidly quenched within a minute to close to room temperature following RTA, the Au solubility may be closer to this value than the equilibrium solubility limit at room temperature of $<1 \times 10^{9}$ cm^{-3} [50]. In terms of the measured optical absorptance, the absorbing layer thickness is now the thickness of the entire wafer ($\sim 500\,\mu$m), and hence the Au substitutional content within this thickness will be approaching 5×10^{12} cm^{-2}, as we discuss later in relation to Fig. 7(b). In addition, we note that Fig. 7(a) shows an apparent

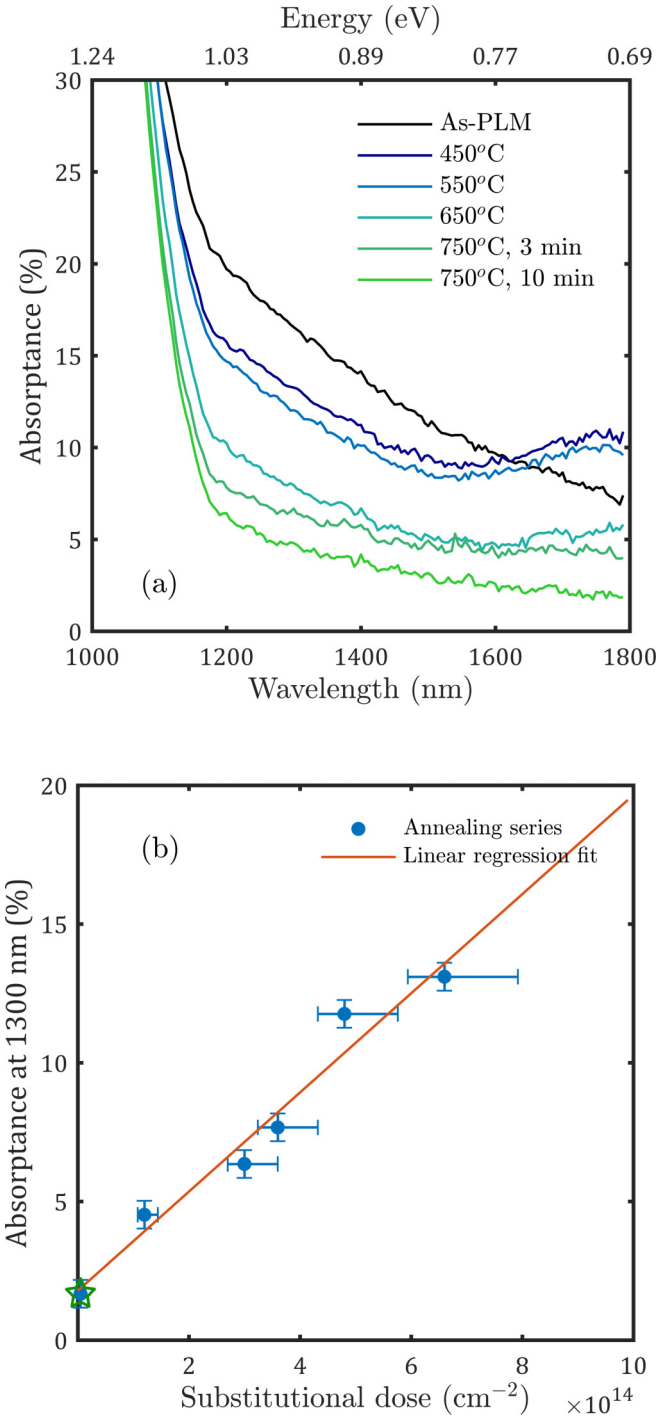

FIG. 7. (a) Sub-Band gap absorptance of the sample implanted to 6×10^{15} cm^{-2} following PLM, and the same sample after RTA at different temperatures. (b) Absorptance of the RTA samples at 1300 nm as a function of substitutional Au dose (measured by RBS/C), and of a reference sample (labeled with a green star), which was implanted with Au to 2×10^{15} cm^{-2} then recrystallized by RTA at 750°C for 3 min. A linear regression fit is also shown. The justification for the size of the error bars is given in Sec. 4 of the Supplemental Material [51].

enhancement in absorptance around 1700 nm for samples that were annealed at temperatures between 450°C and 650°C. The reason for this change in spectral shape is not yet fully understood but is presumably related to lattice distortion and/or residual disorder that is not completely removed during the early stages of Au precipitation. We speculate that such lattice imperfections decrease as the annealing temperature is further increased, causing the absorptance to return to its original spectral shape (i.e., that before thermal deactivation). Thus, any residual absorptance is expected to be dominated by substitutional Au diffused throughout a largely thermally relaxed wafer following RTA at 750°C for 10 min.

Figure 7(b) shows the sub-band gap absorptance measured at 1300 nm as a function of the measured substitutional Au dose, obtained after RTA annealing at various temperatures for the sample implanted to 6×10^{15} cm^{-2}. The linear dependence of sub-band gap absorptance on the substitutional dose is illustrated by a linear fit. We note that the fit shown here does not pass through the origin, implying that an $\sim$1.8% absorptance is expected when the measured substitutional dose is zero as determined by RBS/C. As indicated earlier, we believe this peculiarity arises from the fact that, following RTA, substitutional Au is distributed throughout the entire wafer at a concentration close to the solubility limit associated with the annealing temperature. However, this Au concentration or amount is below the detection limit of RBS/C and, since it is spread throughout the wafer, the sub-band gap absorption coefficient α is expected to be very low. On the other hand, since the absorbing layer thickness t is now more than 1000 times thicker than the original hyperdoped layer ($\sim$500 μm compared with 310 nm), even at such a low Au concentration ($\sim 1 \times 10^{14}$ cm^{-3} at 750°C [49]), the absorption level A ($A \propto \alpha t$) is expected to be small but measureable. To confirm this explanation, we fabricated a sample that was implanted with Au at 2×10^{15} cm^{-2} under identical conditions but was recrystallized directly by RTA at 750°C for 10 min instead of by PLM. In this case, RBS/C showed that almost all of the Au is segregated to the surface during solid-phase epitaxy and no substitutionality was measured (again since the soluble Au distributed through the wafer was below the noise floor of RBS) [52]. As indicated earlier, the equilibrium solubility limit at 750°C would provide an upper limit of the Au substitutional dose of $\sim 5 \times 10^{12}$ cm^{-2}. This RTA annealed sample exhibited 1.7% absorptance at 1300 nm and is plotted as a green star in Fig. 7(b), which is consistent with the fully thermally deactivated samples. Based on this measured absorptance, the absorption coefficient (at 1300 nm) of all samples following RTA at 750°C for 3 min is calculated to be $\leqslant 0.3\,\text{cm}^{-1}$.

Finally, the behavior of the inhomogeneous Au-rich regions after subsequent thermal treatment clearly illustrates their metastability. In particular, the decrease of sub-band gap absorptance with the loss in Au substitutionality highlights the fact that the highly inhomogeneous Au-rich regions contribute strongly to the sub-band gap absorption. These optical absorptance results further reinforce the fact that the inhomogeneous Au-rich filamentary regime investigated in this work is structurally and optically different from conventional, steady-state cellular breakdown, in which Au precipitation and a defective subsurface cellular microstructure are expected to compromise the optical properties of the material.

IV. CONCLUSION

By studying the structure and composition of Au-hyperdoped Si following PLM, we demonstrate an intriguing solidification regime characterized by Au-rich filaments that is fundamentally different from conventional cellular breakdown. Specifically, we show that the Au distribution becomes laterally inhomogeneous when the Au concentration is critically high, but the Au-rich regions continue to exhibit a high degree of Au substitutionality and, correspondingly, high sub-band gap optical activity. In particular, the sub-band gap photoresponse increases with increasing substitutional Au dose regardless of the homogeneity of the Au distribution. This regime of highly concentrated substitutional Au is metastable and precipitates readily during subsequent RTA. In light of these findings, further enhancement in the sub-band gap absorption of Au-hyperdoped Si can be expected if this filamentary regime is fully exploited by optimizing the implantation and PLM conditions. However, the implication of such enhanced infrared absorption for photodetector device performance remains to be addressed. In addition, we anticipate that this regime of inhomogeneous impurity distribution, which is associated with high impurity substitutionality and occurs at lower Au concentrations than that required for conventional, steady-state cellular breakdown, may also be observed in Si hyperdoped with other transition metals. Such behaviors may open the possibility of achieving efficient sub-band gap photoresponse in a broad range of transition-metal-hyperdoped-Si systems.

ACKNOWLEDGMENTS

We acknowledge the Australian Research Council (Grant No. LP160100981) and the US Army (Contract No. FA5209-16-P-0104) for partial financial support of this project. The microscopy work was performed at the ANU node of AMMRF. We acknowledge Prof. Dougal McCulloch from RMIT for the EDS. We further acknowledge access to NCRIS (ANFF and the Heavy Ion Accelerator Capability) facilities at the ANU.

[1] R. A. Soref, Proc. IEEE **81**, 1687 (1993).
[2] X. Wang, Z. Cheng, K. Xu, H. K. Tsang, and J.-B. Xu, Nat. Photonics **7**, 888 (2013).
[3] L. Colace, G. Masini, G. Assanto, H.-C. Luan, K. Wada, and L. Kimerling, Appl. Phys. Lett. **76**, 1231 (2000).
[4] A. Luque and A. Martí, Phys. Rev. Lett. **78**, 5014 (1997).
[5] A. Luque, A. Martí, E. Antolín, and C. Tablero, Phys. B (Amsterdam, Neth.) **382**, 320 (2006).
[6] B. K. Newman, M. J. Sher, E. Mazur, and T. Buonassisi, Appl. Phys. Lett. **98**, 251905 (2011).
[7] P. Baeri, S. U. Campisano, G. Foti, and E. Rimini, J. Appl. Phys. **50**, 788 (1979).
[8] J. A. Kittl, P. G. Sanders, M. J. Aziz, D. P. Brunco, and M. O. Thompson, Acta Metall. **48**, 4797 (2000).
[9] M. J. Aziz and T. Kaplan, Acta Metall. **36**, 2335 (1988).
[10] T. G. Kim, J. M. Warrender, and M. J. Aziz, Appl. Phys. Lett. **88**, 241902 (2006).
[11] M. Tabbal, T. Kim, J. M. Warrender, M. J. Aziz, B. L. Cardozo, and R. S. Goldman, J. Vac. Sci. Technol. B **25**, 1847 (2007).
[12] B. P. Bob, A. Kohno, S. Charnvanichborikarn, J. M. Warrender, I. Umezu, M. Tabbal, J. S. Williams, and M. J. Aziz, J. Appl. Phys. **107**, 123506 (2010).
[13] M. T. Winkler, D. Recht, M.-J. Sher, A. J. Said, E. Mazur, and M. J. Aziz, Phys. Rev. Lett. **106**, 178701 (2011).
[14] E. Ertekin, M. T. Winkler, D. Recht, A. J. Said, M. J. Aziz, T. Buonassisi, and J. C. Grossman, Phys. Rev. Lett. **108**, 026401 (2012).
[15] K. Sánchez, I. Aguilera, P. Palacios, and P. Wahnón, Phys. Rev. B **82**, 165201 (2010).
[16] C. B. Simmons, A. J. Akey, J. J. Krich, J. T. Sullivan, D. Recht, M. J. Aziz, and T. Buonassisi, J. Appl. Phys. **114**, 243514 (2013).
[17] K. Graff, *Metal Impurities in Silicon-Device Fabrication*, Springer Series in Materials Science Vol. 24 (Springer Science and Business Media, New York, 2013).
[18] D. Recht *et al.*, J. Appl. Phys. **114**, 124903 (2013).
[19] J. P. Mailoa *et al.*, Nat. Commun. **5**, 3011 (2014).
[20] C. W. White, S. R. Wilson, B. R. Appleton, and F. W. Young, J. Appl. Phys. **51**, 738 (1980).
[21] D. E. Hoglund, M. O. Thompson, and M. J. Aziz, Phys. Rev. B **58**, 189 (1998).
[22] W. A. Tiller, K. A. Jackson, J. W. Rutter, and B. Chalmers, Acta Metall. **1**, 428 (1953).
[23] W. W. Mullins and R. F. Sekerka, J. Appl. Phys. **35**, 444 (1964).
[24] C. W. White, J. Phys. **44**, 145 (1983).
[25] A. G. Cullis, H. C. Webber, J. M. Poate, and N. G. Chew, J. Microsc. **118**, 41 (1980).
[26] J. W. Mayer and J. M. Poate, *Laser Annealing of Semiconductors* (Academic Press, San Diego, CA, 1982).
[27] J. M. Warrender, J. Mathews, D. Recht, M. Smith, S. Gradečak, and M. J. Aziz, J. Appl. Phys. **115**, 163516 (2014).
[28] A. J. Akey, D. Recht, J. S. Williams, M. J. Aziz, and T. Buonassisi, Adv. Funct. Mater. **25**, 4642 (2015).
[29] J. Narayan, J. Appl. Phys. **52**, 7121 (1981).
[30] J. Narayan, J. Cryst. Growth **59**, 583 (1982).
[31] See Supplemental Material at http://link.aps.org/supplemental/10.1103/PhysRevMaterials.1.074602 for the SAED pattern taken on the cross section of the high-dose sample.
[32] See Supplemental Material at http://link.aps.org/supplemental/10.1103/PhysRevMaterials.1.074602 for an estimation of the Au content in the filaments.
[33] M. J. Aziz, Metall. Mater. Trans. A **27**, 671 (1996).
[34] S. U. Campisano, G. Foti, P. Baeri, M. G. Grimaldi, and E. Rimini, Appl. Phys. Lett. **37**, 719 (1980).
[35] L. R. Doolittle and M. O. Thompson, RUMP Simulation, Cornell University, 1985.
[36] J. S. Williams and R. G. Elliman, *Ion Beams for Materials Analysis* (Academic Press, San Diego, CA, 1989), p. 261.
[37] See Supplemental Material at http://link.aps.org/supplemental/10.1103/PhysRevMaterials.1.074602 for high-resolution XTEM images taken on these samples, with lattice fringes showing slight skewing around the filaments.

[38] A. G. Cullis, N. G. Chew, H. C. Webber, and D. J. Smith, J. Cryst. Growth **68**, 624 (1984).
[39] See Supplemental Material at http://link.aps.org/supplemental/10.1103/PhysRevMaterials.1.074602 for an estimation of the Au content in the filaments.
[40] L. K. Aagesen, A. E. Johnson, J. L. Fife, P. W. Voorhees, M. J. Miksis, S. O. Poulsen, E. M. Lauridsen, F. Marone, and M. Stampanoni, Acta Mater. **59**, 4922 (2011).
[41] K. Tang, E. J. Øvrelid, G. Tranell, and M. Tangstad, *Crystal Growth of Si for Solar Cells* (Springer, New York, 2009), p. 219.
[42] W. Spitzer and H. Y. Fan, Phys. Rev. **108**, 268 (1957).
[43] C. T. Sah, A. F. Tasch, and D. K. Schroder, Phys. Rev. Lett. **19**, 71 (1967).
[44] M. Valdinoci, L. Colalongo, A. Pellegrini, and M. Rudan, IEEE Trans. Electron Devices **43**, 2269 (1996).
[45] P. W. Voorhees, J. Stat. Phys. **38**, 231 (1985).
[46] J. Wong-Leung, E. Nygren, and J. S. Williams, Appl. Phys. Lett. **67**, 416 (1995).
[47] F. H. Baumann and W. Schröter, Phys. Rev. B **43**, 6510 (1991).
[48] S. Coffa, N. Tavolo, F. Frisina, G. Ferla, and S. U. Campisano, Nucl. Instrum. Methods Phys. Res. B **74**, 47 (1993).
[49] C. L. Claeys, R. Falster, M. Watanabe, and P. Stalhofer, *High Purity Silicon 10* (Electrochemical Society, Pennington, NJ, 2008), Vol. 10.
[50] D. M. Jordan, R. H. Haslam, K. Millik, and P. R. Wilshaw, ECS Trans. **16**, 41 (2008).
[51] See Supplemental Material at http://link.aps.org/supplemental/10.1103/PhysRevMaterials.1.074602 for an explanation on how the errors are quantified.
[52] S. H. Lim, W. Mar, P. Matheu, D. Derkacs, and E. T. Yu, J. Appl. Phys. **101**, 104309 (2007).

Supporting Information

1 Lack of precipitation of Au in samples exhibiting filamentary behavior

The SAED pattern of the sample implanted at 300 keV to a Au dose of 6×10^{15} cm^{-2} is shown in **Figure S1**. It contains reflections that can be associated either with the diamond cubic lattice or with twinning of the diamond cubic material, as shown more clearly later in Figure S3. This is in contrast to the SAED obtained from samples after RTA (see Figure 5 and 6), where the additional diffraction spots are clearly not associated with the diamond cubic lattice.

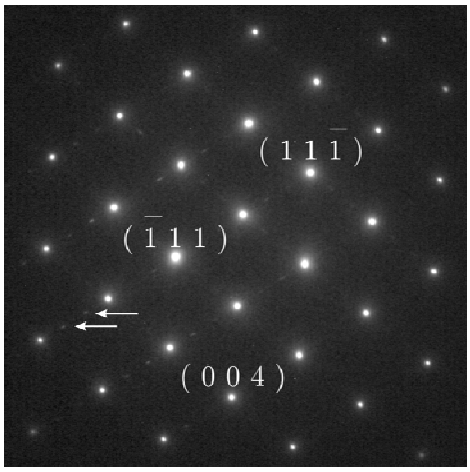

Figure S1 SAED of the sample implanted at 300 keV to a Au dose of 6×10^{15} cm^{-2}. The only additional diffraction spots other than the diamond cubic spots are faint and can be clearly associated with twinning of the lattice (indicated by arrows).

2. Estimation of the Au content in the filaments:

We estimate in this section the Au content inside the Au-rich regions and compare it with the Co case[6]. Although RBS/C is incapable of quantifying the exact concentration of Au inside the individual Au-rich filaments, we base our rough estimate on the peak concentrations measured at ~100-110 nm below the surface. Because no lateral Au inhomogeneity is observed in samples implanted at the dose of 2×10^{15} cm^{-2} or below, we may infer from

Figure 3 (a) that the Au concentration is approximately constant within the top 110 nm at a concentration C_1 = 0.5 × 10^{20} cm^{-3}. For the sample implanted to 6 × 10^{15} cm^{-2}, in which the Au is laterally inhomogeneous, the peak concentration measured at ~100-110 nm from Figure 3 (c), C_2= 7 × 10^{20} cm^{-3}, is the average concentration within this depth range. Hence, the laterally inhomogeneous Au-rich regions must have some other concentration C_B, which is larger than C_2. If we assume that the uniform soluble Au concentration between the Au-rich regions remains at C_1 in the filamentary samples, C_B can be estimated from the fractional volume of the Au-rich regions between 100-110 nm below the surface, *k*:

$$kC_B + (1-k)C_1 = C_2 \,.\# \quad (1)$$

Using the XTEM images, we estimate the value of *k* by dividing the number of pixels in the dark regions by the total number of pixels in the XTEM image cropped to only contain the region ~100 nm to 110 nm below the surface. Applying this method to Figure 2 (b) we find $k \sim 0.3$. This approximation gives an average C_B of ~3 at.% within Au-rich filaments, which is qualitatively consistent with the average impurity concentration in the Co-rich filaments (6 at.%) found in [6]. We emphasize that, similar to the Co case, the Au concentration within different Au-rich regions is likely to vary.

3. Lattice distortion around Au-rich filaments

In supersaturated Si formed by ion implantation and pulsed laser annealing, unidirectional strain normal to the surface can usually be detected by X-ray diffraction (XRD) and Raman spectroscopy. Due to the larger lattice parameter of Au compared with Si, one would expect the strain to be compressive, as is found for Sb in Si [1]. Surprisingly, preliminary XRD and Raman results revealed little significant strain in the Au-hyperdoped layers that contain Au-rich filaments. Although this behavior is interesting and deserves further investigation, it is not the main focus of the current manuscript. Nevertheless, as shown in **Figure S2**, we note

that HRTEM micrographs of the Au-rich filaments indicate distortion in the Si lattice around regions of high mass contrast associated with Au-rich filaments. Such distortions are expected to give rise to a strained local environment in and around the filaments [6, 7].

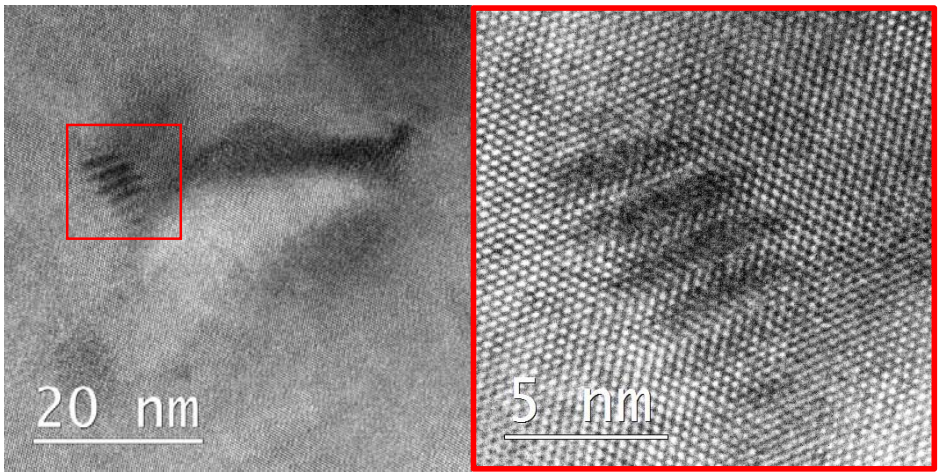

Figure S2 (a) HRTEM (bright field) of the sample implanted to 6×10^{15} cm^{-2} and (b) a magnified view of the region outlined in red, showing lattice fringes that are distorted in the Au-rich filaments.

The sample with the highest Au dose (8×10^{15} cm^{-2}) exhibits a somewhat different behaviour than the others. Although the RBS/C spectra (not shown) are qualitatively similar to the sample implanted to 6×10^{15} cm^{-2}, a much lower measured Au substitutionality of 18% is obtained in the resolidified layer. XTEM on this sample reveals significant twinning in the <111> direction, as shown in **Figure S3**. Since twinning is known to increase the dechannelling rate [2], we expect the measured substitutionality to be affected by the twins as well as strain around the Au-rich regions. In such cases, RBS/C will underestimate the real substitutional fraction of Au within the Au-rich filaments.

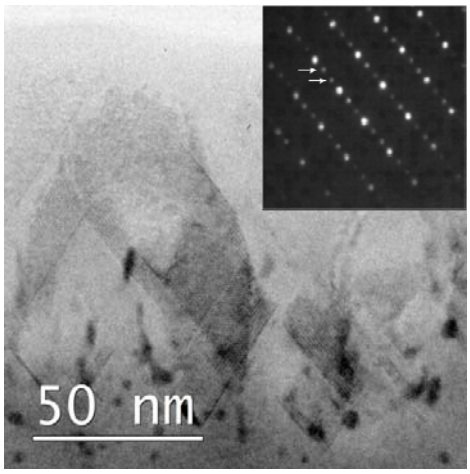

Figure S3 XTEM of the sample implanted to 8×10^{15} cm^{-2} at 300 keV and pulse laser melted at 0.78 $J.cm^{-2}$. Evident twinning appears in the SAED as shown in the inset by the twin spots located at 1/3 and 2/3 spacing between the main diamond cubic spots (indicated by arrows).

4. Estimation of errors from RBS/C

This section justifies our estimation of the error bars for Figure 4 (b) and 7 (b). When calculating the substitutional Au fractions from the random and channelled RBS spectra, we note that sample-to-sample variation in implanted dose, statistical error, pile-up-induced effects and inaccurate geometric alignment can result in a total error of around ±10%. In addition, lattice distortions around the Au-rich regions, as revealed by HRTEM in Figure S2, imply that the He ions impinging on these Au-rich regions will be dechannelled to some extent due to strain in addition to non-substitutionality of Au. Thus, the substitutional Au doses measured here provide a lower bound to the real substitutional Au dose. This underestimation is difficult to quantify exactly but, based on the increase in the Si minimum yield in Figure 3 (c), we estimate an additional 10% error in the positive direction. The vertical error bars in Figure 5 (b) address the *absolute* noise in the measured absorptance, which is estimated to be ±0.5%.

We note that the substitutional Au dose shown in Figure 7 (b) is also expected to be underestimated due to the increased scattering cross-section as a result of the presence of Au precipitates in the lattice. This underestimation is difficult to quantify and for the sake of consistency, an underestimation of 10% has been used. This results in asymmetric error bars which show a +20% and -10% uncertainty.

[1] Y. Takamura, A. Vailionis, A. F. Marshall, P. B. Griffin, and J. D. Plummer, Journal of Applied Physics **92**, 5503 (2002).

[2] G. Foti, L. Csepregi, E. F. Kennedy, J. W. Mayer, P. P. Pronko, and M. D. Rechtin, Nuclear Instruments and Methods **149**, 381 (1978).

[3] L. C. Feldman, J. W. Mayer, and S. T. Picraux, *Materials analysis by ion channeling: submicron crystallography* (Academic Press, 1982).

[4] B. R. Appleton, J. Nabayan, C. W. White, J. S. Williams, and K. T. Short, Nuclear Instruments & Methods in Physics Research **209/210**, 239 (1983).

[5] A. J. Akey, Yang, W., Williams, J.S., Aziz, M. J., Unpublished, 2016.

[6] A. J. Akey, D. Recht, J. S. Williams, M. J. Aziz, and T. Buonassisi, Advanced Functional Materials **25**, 4642 (2015).

[7] J. E. E. Baglin and J. S. Williams, in *Ion Beans for Materials Analysis* (Academic Press, San Diego, 1989), pp. 103.

[8] O. Meyer, H. Mann, and G. Linker, Applied Physics Letters **20**, 259 (1972).